Journal of Materials Chemistry C

ROYAL SOCIETY OF CHEMISTRY

PAPER

View Article Online
View Journal

Cite this: DOI: 10.1039/d3tc00983a

Ordered porous RGO/SnO_2 thin films for ultrasensitive humidity detection†

Zhou Li,[abc] David W. Gardner,[ab] Yong Xia,[abd] Sikai Zhao,[abe] Aifei Pan,[abd] Nishit Goel,[f] Stephen Bart,[f] Chen Liu,[g] Jianxin Yi,[c] Carlo Carraro[ab] and Roya Maboudian *[ab]

Received 20th March 2023,
Accepted 12th June 2023

DOI: 10.1039/d3tc00983a

rsc.li/materials-c

In this work, ordered porous thin films of reduced graphene oxide and tin oxide (rGO/SnO_2) were synthesized by a polystyrene sphere monolayer colloidal crystal template method, and their gas-sensing properties were systematically studied. The formed amorphous SnO_2 and partially reduced graphene oxide were analyzed using several complementary material characterization techniques. The results show that the incorporation of rGO significantly improved the humidity sensitivity and the electrical conductivity of the sensor relative to the pristine SnO_2 thin film. Fast response time and excellent selectivity towards humidity were also achieved for the rGO/SnO_2 composite film. The long-term stability of the rGO/SnO_2 sensor was confirmed by comparing its performance to a commercial humidity sensor. The enhanced sensor performance is attributed to the synergistic effects of the incorporation of rGO and the ordered porous structure of the composite film.

Introduction

Water vapor is the most ubiquitous component of the atmosphere, and its concentration is a crucial parameter to be monitored and controlled for various application areas such as automation industry, medical care, and agriculture production.[1–3] Therefore, highly sensitive and selective sensors for humidity detection have attracted widespread attention. Humidity sensors are mainly classified into capacitive and resistive types in terms of data transduction methods. Although the capacitive-type humidity sensors are commonly used, some of their drawbacks include complicated circuit design, high cost and high-power consumption.[4] Comparatively, resistive-type humidity sensors are attractive due to their low cost, portable size, easy fabrication process, and excellent compatibility with modern electronic devices.[5–8]

As one of the most representative semiconducting metal oxide materials (MOx), tin dioxide (SnO_2) has proven to be a suitable humidity sensing material due to its high sensitivity and excellent electrochemical stability.[9–12] Parthibavarman *et al.* synthesized spherical-shaped SnO_2 nanoparticles using a microwave irradiation method for humidity detection.[9] Yadav *et al.* fabricated nanocrystalline SnO_2 thick film-based humidity sensors using screen printing technique.[10] Zheng *et al.* reported high-sensitivity humidity sensors based on a single SnO_2 nanowire with high concentration of oxygen vacancies synthesized by chemical vapor deposition.[11] However, pristine SnO_2 materials still suffer from several limitations including low electrical conductivity, poor selectivity, and limited measurement range.[13–15] Besides, most research efforts have only focused on highly crystalline SnO_2 synthesized at high temperatures (350–700 °C) with tetragonal rutile structures, and amorphous SnO_2 formed at temperatures below 200 °C have not been investigated for humidity detection purposes.[16,17]

In recent years, graphene has attracted significant research interest for sensing applications due to its large specific surface area and high electrical conductivity.[18–20] However, due to the absence of functional groups and defect sites, graphene often exhibits poor sensing performance.[21,22] Reduced graphene oxide (rGO), a common graphene derivative, is considered to be a promising sensing material mainly because of its abundant surface functional groups and facile synthesis process.[23,24] Notably, rGO/SnO_2 nanocomposites have emerged as a new

[a] Department of Chemical and Biomolecular Engineering, University of California, Berkeley, California, 94720, USA. E-mail: maboudia@berkeley.edu
[b] Berkeley Sensor & Actuator Center, University of California, Berkeley, California, 94720, USA
[c] State Key Laboratory of Fire Science, Department of Safety Science and Engineering, University of Science and Technology of China, Hefei, Anhui 230026, P. R. China
[d] School of Mechanical Engineering, Xi'an Jiaotong University, Xi'an, Shanxi 710049, P. R. China
[e] School of Resources and Civil Engineering, Northeastern University, Shenyang, Liaoning 110819, P. R. China
[f] TDK InvenSense Inc., San Jose, California, 95110, USA
[g] Department of Mechanical Engineering, Stanford University, Stanford, CA 94305, USA

† Electronic supplementary information (ESI) available. See DOI: https://doi.org/10.1039/d3tc00983a

class of gas-sensing materials. Zhang *et al.* synthesized SnO_2 nanoparticle-loaded rGO by hydrothermal method and achieved highly sensitive NO_2 detection at low operating temperature (50 °C).[25] Liu *et al.* achieved sensitive room-temperature H_2S detection and low cross-sensitivity to common interfering gases including NO_2 and NH_3 using SnO_2 quantum wire/rGO nanocomposites.[26] Rao *et al.* fabricated room-temperature liquid propane gas sensors by employing rGO/SnO_2 nanocomposites as sensing materials.[27] These reports highlighted that graphene/SnO_2 nanocomposites exhibit a large enhancement in gas-sensing properties in comparison with either pure SnO_2 or rGO.

In this work, the polystyrene sphere monolayer colloidal crystals (PSMCC) template method is adopted to synthesize ordered porous rGO/SnO_2 thin films. A low annealing temperature of 120 °C is selected for forming amorphous SnO_2 and partially reduced graphene oxide. Humidity-sensing properties of the thin films are systematically examined. Gas exposure tests show that rGO/SnO_2 nanocomposite film demonstrates superior humidity-sensing performance compared to pristine rGO and SnO_2 films due to the unique film microstructure and promoting effect of rGO. The rGO/SnO_2 material also shows high selectivity and long-term stability. The sensing behaviour and mechanism of the rGO/SnO_2 nanocomposite material are also discussed.

Results and discussion

Material properties and microstructure

X-ray diffraction was employed to probe the structure of the synthesized rGO/SnO_2 (Fig. 1). By evaporating and annealing the corresponding precursor solutions, SnO_2, rGO, and rGO/SnO_2 powder samples were also obtained for XRD measurements. For comparison, XRD patterns of $SnCl_4{\cdot}5H_2O$ precursor and GO precursor powders were also examined. As shown in Fig. 1, compared to the XRD pattern of $SnCl_4{\cdot}5H_2O$ precursor, SnO_2 powder sample only exhibits two broad diffraction peaks of low crystallinity at 31° and 54°, respectively, and no other diffractions peaks are identified, indicating its amorphous feature.[28,29] The conversion from $SnCl_4{\cdot}5H_2O$ to amorphous SnO_2 is also consistent with the TGA and DTG results of $SnCl_4{\cdot}5H_2O$ in air that report the largest weight loss in the range of 80–160 °C (Fig. S1a, ESI†). The *d*-spacing is calculated to be 8.1 Å for GO and 7.1 Å for rGO based on the strong and sharp (002) peaks at 11.0° and 12.4°, respectively.[30,31] After the thermal reduction, the main peak shifts towards higher angles, indicating a decrease in *d*-spacing and an increase in stacking of graphene sheets, and consistent with prior reports.[31] The conversion from GO to rGO is also consistent with the TGA and DTG results of GO in air that showed a large weight loss in the range of 30–150 °C (Fig. S1b, ESI†). The rGO/SnO_2 composite exhibits two broad diffraction peaks of low crystallinity from amorphous SnO_2 but no peaks from rGO, which is mainly ascribed to low weigh ratio (1.4%) of GO to $SnCl_4{\cdot}5H_2O$ in the precursor solution.

Fig. 2 shows the FTIR spectra of $SnCl_4{\cdot}5H_2O$, SnO_2, GO, rGO, and rGO/SnO_2. The $SnCl_4{\cdot}5H_2O$ sample shows stretching vibrations of the O–H bond at around 3500 cm^{-1} and bending vibrations of H–O–H at around 1600 cm^{-1}. The absorption bands below 900 cm^{-1} are related with the vibrations of Sn–Cl bonds.[32] In comparison, the SnO_2 sample exhibits the stretching vibrations of Sn–O at around 510 cm^{-1} and the symmetric vibrations of O–Sn–O at around 670 cm^{-1}, respectively.[33] The raw GO sample displays the presence of bands associated to C–O at 1053 cm^{-1}, C–O–C at 1270 cm^{-1}, C–OH at 1416 cm^{-1}, C═C at 1630 cm^{-1}, C═O at 1733 cm^{-1}, and O–H bonds at 3500 cm^{-1}, respectively.[34] In comparison, the lower intensity of C–O, C–OH, and C═O vibrations and higher intensity of C–O–C of rGO sample suggests partial reduction of oxygen-containing functional groups of GO by annealing. The rGO/SnO_2 composite exhibits various vibration peaks from SnO_2 but no peaks from rGO due to the low concentration of GO in the precursor solution.

Fig. 3 shows the Raman spectra of $SnCl_4{\cdot}5H_2O$, SnO_2, GO, rGO, and rGO/SnO_2 samples. The $SnCl_4{\cdot}5H_2O$ sample shows peaks at 155 cm^{-1} and 326 cm^{-1} corresponding to the Cl–Sn–Cl asymmetric bending and the Sn–Cl symmetric stretching, respectively.[35] For SnO_2 sample, these two peaks disappear but a broad peak is observed at around 350 cm^{-1}, which is ascribed

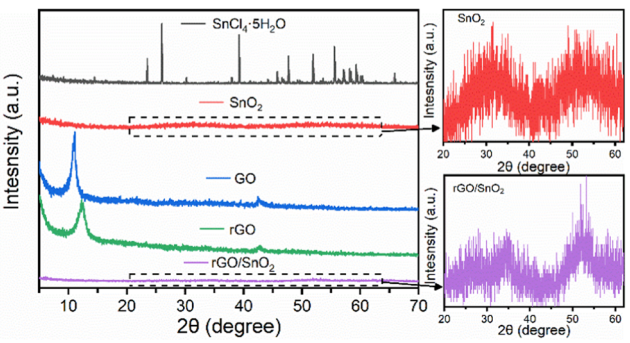

Fig. 1 XRD patterns of $SnCl_4{\cdot}5H_2O$, SnO_2, GO, rGO, and rGO/SnO_2.

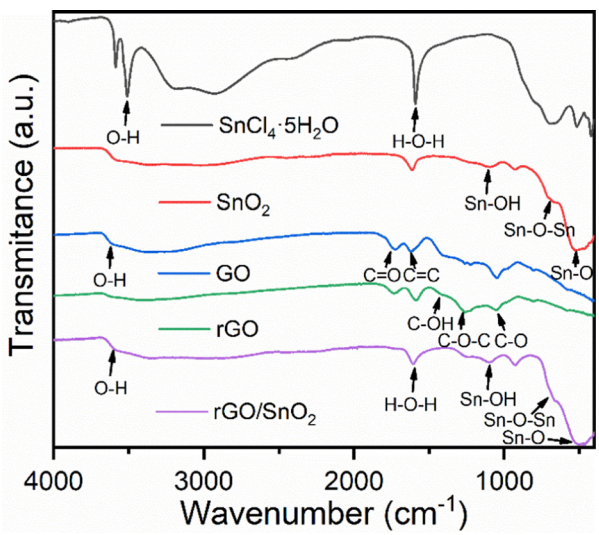

Fig. 2 FTIR spectra of $SnCl_4{\cdot}5H_2O$, SnO_2, GO, rGO, and rGO/SnO_2.

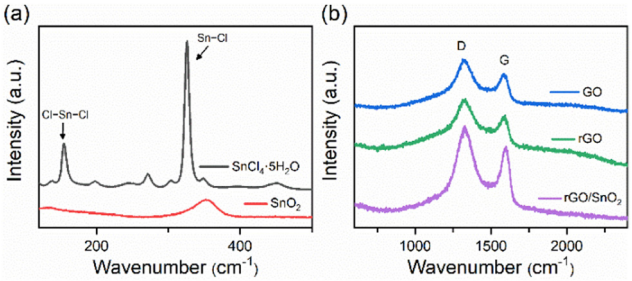

Fig. 3 Raman spectra of (a) $SnCl_4·5H_2O$, SnO_2, and (b) GO, rGO, and rGO/SnO_2.

to the formation of amorphous SnO_2 nanoclusters by annealing.[36] The GO and rGO samples both have two prominent peaks corresponding to D and G bands at ~1323 and ~1585 cm^{-1}, respectively. No obvious peak shift is observed by comparing the peak positions of each sample. In addition, no obvious trend in the intensity ratio of D to G bands is observed, which implies that annealing at a low temperature, 120 °C, does not introduce defects detectable by Raman spectroscopy. For the rGO/SnO_2 composite, the two main peaks from the D and G bands of graphene are observed but no peaks from SnO_2 are located, which is ascribed to the low intensity for vibrations of amorphous SnO_2.

Scanning electron microscopy was used to observe the morphologies and microstructures of polystyrene template, SnO_2/PS, rGO/PS, and rGO/SnO_2/PS films deposited on Si(100) substrate and annealed at 120 °C. The relatively brighter particles observed are attributed to the Au/Pd nanoalloy sputter deposited for enhancing the conductivity of the sample for SEM imaging. As can be seen from Fig. 4a and e, the PS monolayer colloidal crystals template melt and form a thin film after annealing. The formed PS film was identified by Raman spectroscopy (Fig. S2a, ESI†). For SnO_2/PS film, homogeneous ordered arrays over a large region are observed (Fig. 4b). The corresponding high-magnification SEM image confirmed ordered quasi-hexagon skeletons of 500 nm diameter established by the PS sphere size (Fig. 4f). Besides the Au/Pd nanoalloy, the existence of polystyrene was also confirmed by Raman spectroscopy (Fig. S2a, ESI†). Compared to SnO_2/PS film, the rGO/PS film shows less ordered structure (Fig. 4c and g). The rGO/SnO_2/PS film exhibits desired ordered porous structure, as shown in Fig. 4d and h. From the inset of Fig. 4h, the thickness of the RGO/SnO_2/PS film is estimated to ~3 μm. The details of the cross section of the RGO/SnO_2/PS film can be observed in Fig. S3 (ESI†). Only graphene peaks and no polystyrene-associated peaks were observed by Raman spectroscopy carried out on the RGO/SnO_2/PS and rGO/PS films (Fig. S2b, ESI†). This result might be ascribed to much higher sensitivity of Raman to graphene over polystyrene, leading to the absence of polystyrene in these spectra.

Gas-sensing properties

Fig. 5 shows the room-temperature response of the rGO/SnO_2/PS sensor *vs.* relative humidity. For comparison, the responses of the sensors based on constituent components, namely, PS, SnO_2/PS, rGO/PS, are also shown. The resistance values of all the sensors decrease as the relative humidity increases. However, except for the close high resistance values in dry air, the sensors exhibit quite different behavior at high humidity. In particular, the rGO/SnO_2/PS sensor shows the steepest decrease, indicating its highest electrical conductivity and humidity sensitivity.

The sensors were also exposed to exhaled breath and finger humidity to present their dynamic response capacities at an ambient relative humidity of 35%. As can be seen from Fig. 6a, when the rGO/SnO_2/PS sensor is exposed to exhaled breath, the resistance very rapidly decreases, and starts to recover to the baseline when exhaled breath is stopped. During the continuous measurement cycles, not only the response and recovery transients but also the baseline values are highly repeatable. Fig. 6b shows the response of rGO/SnO_2/PS sensor to finger humidity. When an index finger is placed over the sensor, the resistance decreases quickly, and recovers back to baseline after the finger is removed. During the continuous measurement cycles, this response–recovery behavior can be well repeated, indicating its potential application for sensing noncontact skin breathing.[37,38] As a possible application, the sensor may be applied as a noncontact switch, which is useful to prevent the spread of the ongoing coronavirus disease. Compared to the

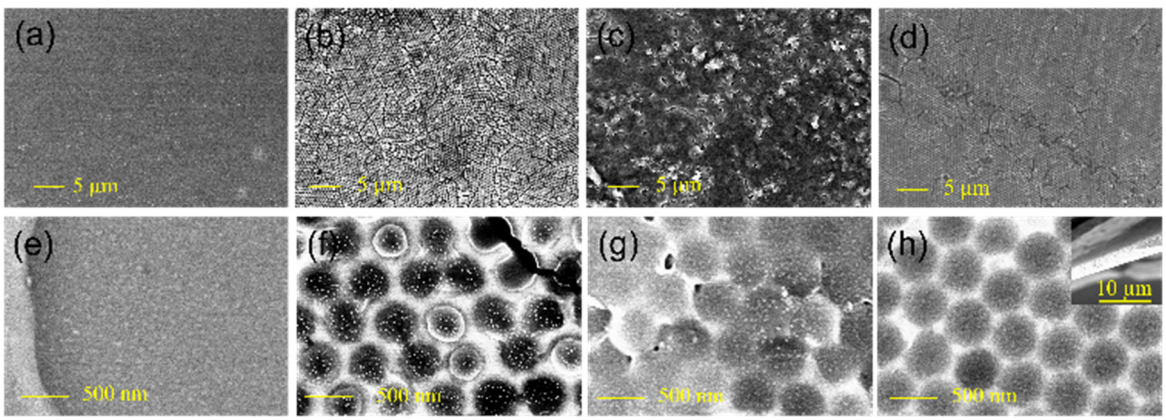

Fig. 4 Low- and high-magnification SEM images of (a and e) PS, (b and f) SnO_2/PS, (c and g) rGO/PS, and (d and h) rGO/SnO_2/PS. Inset in (h) is the corresponding cross section of rGO/SnO_2/PS.

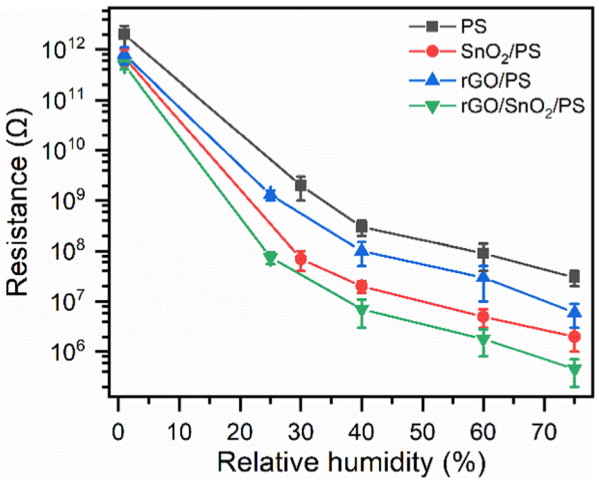

Fig. 5 Electrical resistances of PS, SnO_2/PS, rGO/PS, and rGO/SnO_2/PS sensor as function of relative humidity at room temperature.

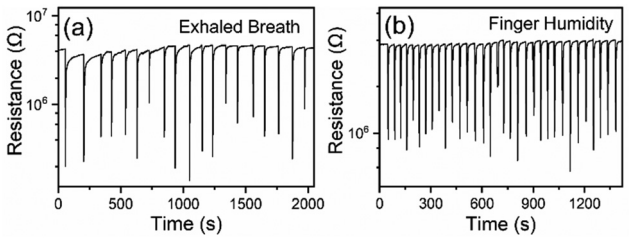

Fig. 6 Dynamic resistance changes of rGO/SnO_2/PS sensor at an ambient relative humidity of 35% to (a) exhaled breath and (b) finger humidity.

performance of rGO/SnO_2/PS sensor, PS sensor exhibits longer recovery time and less stable baseline (Fig. S4a and S5a, ESI†), while rGO/PS, and rGO/SnO_2/PS sensors show higher resistance and lower humidity sensitivity (Fig. S4b, c and S5b, c, ESI†).

To quantitatively analyze the response and recovery behaviors, the performance of rGO/SnO_2/PS sensor exposed to 75% R.H. humidified air was measured under an ambient relative humidity of 25%. As can be seen from Fig. S6 (ESI†), during the continuous measurement cycles, not only the response and recovery transients are fast but also the baseline recovery of the sensor is excellent. The response time of the sensor is calculated to be 1.4 s, which is extremely short, as shown in Fig. 7. The recovery time of the sensor is calculated to be 335 s. In contrast, the rGO/PS sensor cannot recover to the baseline value after several measurement cycles (Fig. S7, ESI†), indicating that SnO_2 is critical to the stability of rGO/SnO_2/PS sensor. In addition, given the operating temperature of room temperature, the amorphous nature of SnO_2 should affect the stability of the sensor much less than at elevated temperatures.

To analyze the selectivity of the rGO/SnO_2/PS sensor, the sensor response to several interfering gases is investigated (Fig. 8). CO_2 and CH_4 are selected as typical greenhouse gases, which might vary significantly in certain natural environments. Ethanol is selected due to its strong interference to traditional SnO_2 based gas sensors. Concentration of 5000 ppm is chosen

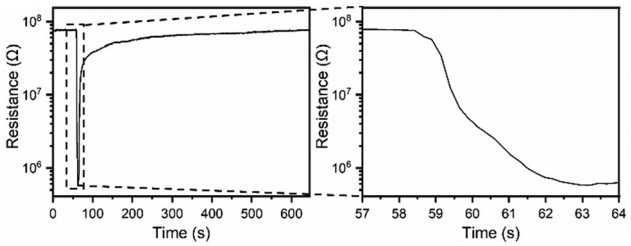

Fig. 7 Response and recovery behavior of rGO/SnO_2/PS sensor to 75% R.H. humidified air at an ambient relative humidity of 25%.

for CO_2 and CH_4 as it exceeds the maximum concentration that most environments can reach. Concentration of 500 ppm is chosen for ethanol as it exceeds the minimum identifiable odor level of approximately 350 ppm for human beings.[39] Similar to humidity, the sensor resistance to methane and ethanol is found to decrease while the sensor resistance in response to CO_2 is found to increase. This sensing behavior is consistent with related literature.[40–42] As can be seen from Fig. 8, the response of the sensor to 40% R.H. humidified air is calculated to be around 71 000 ± 12 890, significantly higher than those to the selected interfering gases (Fig. S9, ESI†). Specifically, while the responses to CO_2, ethanol, and methane vary with relative humidity, they all remain below 4, indicating the excellent selectivity of rGO/SnO_2/PS sensor to relative humidity. In addition, the selectivity of rGO/SnO_2 sensor (without PS monolayer template) was also evaluated (Fig. S8 and S10, ESI†). The response of rGO/SnO_2 sensor to 40% R.H. humidified air (6300 ± 980) is significantly lower than that of rGO/SnO_2/PS sensor, indicating that the ordered porous structure generated by PS monolayer template can efficiently enhance the sensing performance of rGO/SnO_2 composite.

The stability of rGO/SnO_2 sensor is evaluated by comparing its performance with the commercial BME280 humidity sensor. The dynamic conductivity changes of rGO/SnO_2 sensor were first measured as relative humidity was manually controlled to fluctuate greatly within a 3 h time window. As can be seen from Fig. 9a, while the relative humidity fluctuates from 0 to 85%, the conductivity changes of rGO/SnO_2 sensor are highly consistent with the relative humidity changes detected by BME280 sensor. In addition, rGO/SnO_2/PS sensor exhibits even faster response speed in some cases which are highlighted by dashed circles in Fig. 9a. The dynamic conductivity changes of rGO/SnO_2 sensor were then measured as relative humidity naturally changed in an indoor space over an 8 day period. As can be seen

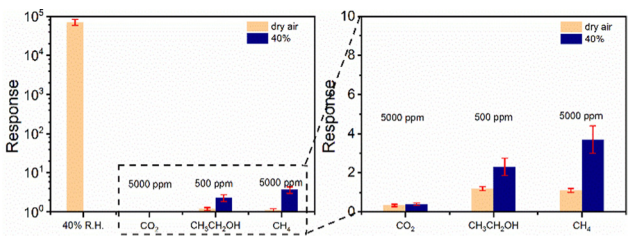

Fig. 8 Responses of rGO/SnO_2/PS sensor to 40% R.H. humidified air as well as CO_2, ethanol, and methane in dry and 40% R.H. humidified air.

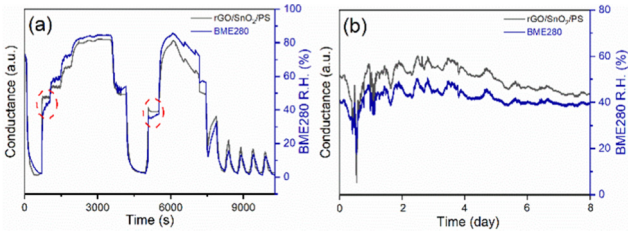

Fig. 9 (a) Dynamic conductivity changes of rGO/SnO_2/PS sensor as relative humidity is manually controlled to fluctuate over 3 hours and (b) as relative humidity naturally changes in an indoor space over 8 days.

from Fig. 10b, the conductivity changes of rGO/SnO_2 sensor match well with the relative humidity changes detected by the commercial sensor. These results demonstrate the excellent stability of rGO/SnO_2/PS sensor.

The above results demonstrate that the rGO/SnO_2/PS sensor sensor in this present work possessed excellent overall humidity-sensing performance. When compared with related humidity sensors, the rGO/SnO_2/PS exhibited markedly higher response value and shorter response time (Table S1, ESI†).

We propose the following mechanism for the observed behavior of the rGO/SnO_2/PS sensor to relative humidity, as shown by Fig. 10. The humidity sensing mechanism is highly associated with the electrical conduction of rGO/SnO_2/PS thin film surface under the exposure to humidity.[19,43,44] Under low-humidity conditions, water molecules in the form of hydroxyl groups are chemically adsorbed on the surface of rGO/SnO_2/PS thin film. As the relative humidity increases, more water molecules can be physically adsorbed. The adsorbed water molecules form a continuous mobile water layer on the film surface. A fraction of absorbed water molecules can be ionized by an external electric field and form hydronium ions (H_3O^+) as charge carriers by Grotthuss chain reaction ($H_2O + H_3O^+ \rightarrow H_3O^+ + H_2O$), which has been widely accepted as proton hopping behavior.[12,14] Under high-humidity conditions, multilayer physisorption of water vapor promotes the proton transfer and penetration into the rGO/SnO_2/PS thin film, leading to a large increase in the conduction. We further hypothesize that the incorporation of rGO into SnO_2/PS thin film creates more active sites, resulting in the adsorption of more water molecules, thus leading to the higher response value, faster response speed, and better selectivity with higher conductivity in response to humidity.

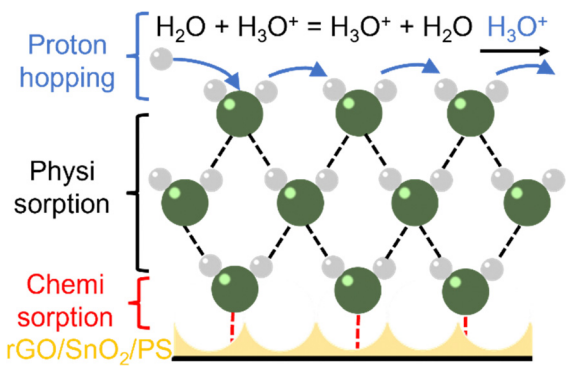

Fig. 10 Schematic diagram of humidity sensing mechanism.

Conclusions

In this work, porous rGO/SnO_2 thin films were synthesized by the PSMCC template method. The incorporation of rGO into SnO_2 thin film creates more active sites, which favors adsorption water molecules, leading to higher, faster and selective response, with higher electrical conductivity than the individual material components. The excellent stability of rGO/SnO_2 thin film was confirmed by comparing the performance to a commercial humidity sensor. The formed ordered porous structure was found to be critical to the excellent humidity-sensing performance. A proton conduction mechanism based on Grotthuss chain reaction has been proposed to explain the observed behavior.

Experimental details

Synthesis of materials and sensor preparation

In this work, the polystyrene sphere monolayer colloidal As shown in Fig. S11 (ESI†), ordered, porous SnO_2, rGO, and rGO/SnO_2 films were synthesized by a modified PSMCC template method originally presented elsewhere.[45,46] Briefly, 3.50 g of tin(IV) chloride pentahydrate ($SnCl_4 \cdot 5H_2O$) and 50 mg of graphene oxide (lateral dimension, 300–800 nm, Cheaptubes, Inc.) were sonicated in 100 mL of deionized water to prepare the precursor solution. A glass substrate covered with PSMCC template (Microgenics Corporation, 500 nm diameter, 10.0 wt% in water) was fabricated by gas–liquid–solid interface self-assembly method.[45] As the glass substrate was gradually immersed into the precursor solution, the colloidal template was stripped off from it and floated on the precursor by the buoyancy force (Fig. S11a, ESI†). The floating template was picked up by the sensing platform which consists of Au interdigitated electrodes (electrode width: 200 μm; separation: 200 μm) deposited on an alumina substrate (8 × 10 mm^2) (Fig. S11b, ESI†). After drying at room temperature overnight, GO/tin chloride based thin films with ordered PS arrays were formed (Fig. S11c, ESI†). Finally, rGO/SnO_2 ordered porous films were obtained after annealing at 120 °C for 3 h in ambient laboratory air (Fig. S11d, ESI†). The obtained sensors are hereafter denoted as rGO/SnO_2/PS.

To compare the sensors to those made from their individual components, SnO_2 and rGO ordered porous films were also prepared by employing pure tin chloride and graphene oxide solutions as the precursors, respectively. The obtained samples are hereafter denoted as SnO_2/PS and rGO/PS, respectively. Polystyrene thin films were also prepared by employing only deionized (DI) water as the solvent. The obtained sample is hereafter denoted as PS. To demonstrate the benefits of the ordered porous structure, rGO/SnO_2 thin films were also prepared without using the PSMCC template for comparison. The obtained sample is hereafter denoted as rGO/SnO_2. Two conductive Pt wires were connected to the Au electrodes with silver epoxy for further gas-sensing measurement.

Characterizations

The crystal structure of the samples was investigated by powder X-ray diffraction (PXRD, Cu Kα radiation, λ = 1.54 Å, 40 kV, 40 mA). The morphologies of the samples were acquired using field-emission scanning electron microscopy (FESEM, Hitachi S-5000). A thin Au/Pd layer was sputter deposited on the samples to improve the electrical conductivity to the material prior to SEM imaging. The chemical status of the samples was evaluated by Raman spectroscopy (Horiba LabRAM confocal Raman spectrometer) with an excitation laser of 632.8 nm and Fourier transform infrared (FTIR) spectroscopy (VERTEX 80, Bruker) in the range of 4000–400 cm^{-1}. The thermal stability was studied using thermogravimetric analysis (TGA, TA Instrument SDT 650) with a ramping rate of 20 °C min^{-1} in air.

Gas sensing measurements

The gas sensing manifold was detailed in our previous report.[8] The prepared interdigitated Au electrode-based sensors (Weisheng Electronics Co. Ltd, China) were placed on a circular miniature heater with a diameter of 5 mm in a homemade stainless-steel test chamber of ~13 mL control volume. Two-point probe resistance of the sensor was measured using a Keithley 2602 controlled by a Java-based program, Zephyr. The gas flow rates were controlled by mass flow controllers (MFC, Bronkhorst) controlled by a LabView program, with a total flow rate kept at 300 sccm. The target gas was diluted with pre-dried house air to reach a specific concentration and then delivered to the test chamber. To probe the sensor recovery, the flow of the gas was shut off so that the sensors were exposed to air again. Humidity concentration was controlled by varying the flow rate of air through a bubbler containing water at room temperature (22 ± 2 °C). The tested interfering gases included ethanol (Airgas, 978 ppm in N_2), CO_2 (Airgas, 5.038% in N_2), and CH_4 (Airgas, 5% in N_2). The sensor response was defined as R_a/R_g, where R_a and R_g were the sensor resistances in dry air and humidified air, respectively. The response (recovery) time was defined as the time that the resistance variation reached 90% of the total value after introduction (or removal) of the analyte gas. Exhaled breath and index finger were controlled carefully as humidity source for qualitative measurements. The distance between the finger and sensor was maintained as well as possible to be around 2 mm.

Long-term stability evaluation was carried out by comparing our rGO/SnO_2/PS humidity sensor with a commercial humidity sensor (BME280, Bosch Sensortec) connected to a Raspberry Pi platform controlled by a Python-based program in an indoor space (Fig. S12, ESI†).

Author contributions

Zhou Li: conceptualization, investigation, writing – original draft. David W. Gardner: investigation, writing – review & editing. Yong Xia: investigation, writing – review & editing. Sikai Zhao: investigation, writing – review & editing. Aifei Pan: investigation, writing – review & editing. Nishit Goel: investigation, writing – review & editing. Stephen Bart: investigation, writing – review & editing. Chen Liu: investigation, writing – review & editing. Jianxin Yi: investigation, supervision, writing – review & editing. Carlo Carraro: investigation, supervision, writing – review & editing. Roya Maboudian: investigation, funding acquisition, resources, supervision, writing – review & editing.

Conflicts of interest

The authors declare no competing financial interest.

Acknowledgements

The authors gratefully acknowledge the support of the National Science Foundation (grant #1903188 and 1929447) and the industrial members of the Berkeley Sensor & Actuator Center. The authors thank Matthew Dods for the XRD measurements. Work at the Molecular Foundry was supported by the Office of Science, Office of Basic Energy Sciences, of the U.S. Department of Energy under Contract No. DE-AC02-05CH11231. Z.L. acknowledges the additional support from the China Scholarship Council.

References

1 H. Farahani, R. Wagiran and M. N. Hamidon, *Sensors*, 2014, **14**, 7881–7939.
2 Y. Zhao, R. J. Tong, M. Q. Chen and F. Xia, *Sens. Actuators, B*, 2019, **284**, 96–102.
3 T. Delipinar, A. Shafique, M. S. Gohar and M. K. Yapici, *ACS Omega*, 2021, **6**, 8744–8753.
4 S. Y. Park, Y. H. Kim, S. Y. Lee, W. Sohn, J. E. Lee and D. H. Kim, *et al.*, *J. Mater. Chem. A*, 2018, **6**, 5016–5024.
5 Y. H. Kim, S. J. Kim, Y. J. Kim, Y. S. Shim, S. Y. Kim and B. H. Hong, *et al.*, *ACS Nano*, 2015, **9**, 10453–10460.
6 D. I. Lim, J. R. Cha and M. S. Gong, *Sens. Actuators, B*, 2013, **183**, 574–582.
7 S. P. Xu, F. Q. Sun, F. L. Gu, Y. B. Zuo, L. H. Zhang and C. F. Fan, *et al.*, *ACS Appl. Mater. Interfaces*, 2014, **6**, 1251–1257.
8 S. K. Zhao, Y. Xia, S. DelaCruz, A. F. Pan, Z. Li and Y. B. Shen, *et al.*, *Ceram. Int.*, 2022, **48**, 6835–6841.
9 M. Parthibavarman, V. Hariharan and C. Sekar, *Mater. Sci. Eng., C*, 2011, **31**, 840–844.
10 B. C. Yadav, R. Singh and S. Singh, *J. Exp. Nanosci.*, 2013, **8**, 506–519.
11 Q. Kuang, C. S. Lao, Z. L. Wang, Z. X. Xie and L. S. Zheng, *J. Am. Chem. Soc.*, 2007, **129**, 6070–6071.
12 V. Solanki, S. B. Krupanidhi and K. K. Nanda, *ACS Appl. Mater. Interfaces*, 2017, **9**, 41428–41434.
13 D. Z. Zhang, H. Y. Chang, P. Li, R. H. Liu and Q. Z. Xue, *Sens. Actuators, B*, 2016, **225**, 233–240.
14 D. Z. Zhang, Y. E. Sun, P. Li and Y. Zhang, *ACS Appl. Mater. Interfaces*, 2016, **8**, 14142–14149.
15 J. S. Tawale, G. Gupta, A. Mohan and A. Kumar, *Sens. Actuators, B*, 2014, **201**, 369–377.

16 V. Paolucci, J. De Santis, L. Lozzi, G. Giorgi and C. Cantalini, *Sens. Actuators, B*, 2022, **350**, 130890.
17 J. Barbe, M. L. Tietze, M. Neophytou, B. Murali, E. Alarousu and A. El Labban, *et al.*, *ACS Appl. Mater. Interfaces*, 2017, **9**, 11828–11836.
18 H. Long, A. Harley-Trochimczyk, T. Pham, Z. R. Tang, T. L. Shi and A. Zettl, *et al.*, *Adv. Funct. Mater.*, 2016, **26**, 5158–5165.
19 D. Burman, R. Ghosh, S. Santra and P. K. Guha, *RSC Adv.*, 2016, **6**, 7424–7433.
20 Q. G. Shao, J. Tang, Y. X. Lin, F. F. Zhang, J. S. Yuan and H. Zhang, *et al.*, *J. Mater. Chem. A*, 2013, **1**, 15423–15428.
21 G. C. Mastrapa and F. L. Freire, *J. Sens.*, 2019, 5492583.
22 W. C. Tian, X. H. Liu and W. B. Yu, *Appl. Sci.*, 2018, **8**, 1118.
23 K. Toda, R. Furue and S. Hayami, *Anal. Chim. Acta*, 2015, **878**, 43–53.
24 A. Lipatov, A. Varezhnikov, P. Wilson, V. Sysoev, A. Kolmakov and A. Sinitskii, *Nanoscale*, 2013, **5**, 5426–5434.
25 H. Zhang, J. C. Feng, T. Fei, S. Liu and T. Zhang, *Sens. Actuators, B*, 2014, **190**, 472–478.
26 Z. L. Song, Z. R. Wei, B. Wang, Z. Luo, S. M. Xu and W. K. Zhang, *et al.*, *Chem. Mater.*, 2016, **28**, 1205–1212.
27 S. Goutham, S. Bykkam, K. K. Sadasivuni, D. S. Kumar, M. Ahmadipour and Z. A. Ahmad, *et al.*, *Microchim. Acta*, 2018, **185**, 69.
28 X. H. Liu, J. Zhang, W. P. Si, L. X. Xi, S. Ostwald and C. L. Yan, *et al.*, *Nanoscale*, 2015, **7**, 282–288.
29 M. P. Subramaniam, G. Arunachalam, R. Kandasamy, P. Veluswamy and I. Hiroya, *J. Mater. Sci.: Mater. Electron.*, 2018, **29**, 658–666.
30 Y. Sheng, X. S. Tang, E. W. Peng and J. M. Xue, *J. Mater. Chem. B*, 2013, **1**, 512–521.
31 S. H. Huh, *Phys. Appl. Graphene: Exp.*, 2011, 73–90.
32 S. A. Trujillo, D. Pena-Solorzano, O. R. Bejarano and C. Ochoa-Puentes, *RSC Adv.*, 2020, **10**, 40552–40561.
33 K. C. Suresh, S. Surendhiran, P. M. Kumar, E. R. Kumar, Y. A. S. Khadar and A. Balamurugan, *SN Appl. Sci.*, 2020, **2**, 1735.
34 B. D. Ossonon and D. Belanger, *RSC Adv.*, 2017, **7**, 27224–27234.
35 W. G. Zhu, T. K. Yao, J. H. Shen, W. Q. Xu, B. W. Gong and Y. C. Wang, *et al.*, *J. Phys. Chem. C*, 2019, **123**, 9575–9581.
36 M. N. Rumyantseva, A. M. Gaskov, N. Rosman, T. Pagnier and J. R. Morante, *Chem. Mater.*, 2005, **17**, 893–901.
37 J. X. Dai, H. R. Zhao, X. Z. Lin, S. Liu, Y. S. Liu and X. P. Liu, *et al.*, *ACS Appl. Mater. Interfaces*, 2019, **11**, 6483–6490.
38 Z. H. Duan, Y. D. Jiang, M. G. Yan, S. Wang, Z. Yuan and Q. N. Zhao, *et al.*, *ACS Appl. Mater. Interfaces*, 2019, **11**, 21840–21849.
39 National Research Council. *The National Academies Press*, 1996, **3**, 171.
40 N. Pienutsa, P. Roongruangsree, V. Seedokbuab, K. Yannawibut, C. Phatoomvijitwong and S. Srinives, *Nanotechnology*, 2021, **32**, 115502.
41 S. Navazani, A. Shokuhfar, M. Hassanisadi, M. Askarieh, A. D. Carlo and A. Agresti, *Talanta*, 2018, **181**, 422–430.
42 S. E. Zaki, M. A. Basyooni, M. Shaban, M. Rabia, Y. R. Eker, G. F. Attia, M. Yilmaz and A. M. Ahmed, *Sens. Actuators, B*, 2019, **294**, 17–24.
43 P. G. Su and C. F. Chiou, *Sens. Actuators, B*, 2014, **200**, 9–18.
44 S. Y. Park, Y. Kim, T. Kim, T. H. Eom, S. Y. Kim and H. W. Jang, *InfoMat*, 2019, **1**, 289–316.
45 Z. Li and J. X. Yi, *Sens. Actuators, B*, 2020, **317**, 128217.
46 H. Zhang, Z. Li, J. X. Yi, H. Zhang and Z. B. Zhang, *Sens. Actuators, B*, 2020, **321**, 128505.